Worldview-02 offers new capabilities for the monitoring of threatened coral reefs

Jeremy M. Kerr
Nova Southeastern University – National Coral Reef Institute
Email: jk908@nova.edu

Research highlights

Worldview-02 increases the number of spectral bands from the traditional 4 in the visible and near-infrared spectrum to 8 bands, and in doing so, provides much enhanced capability for work on coral reefs. Specifically, this increase facilitates more accurate optical derivation of water depth from the satellite imagery. Such bathymetry products are needed to answer key questions on the fate of these threatened ecosystems. This study demonstrates pre-processing techniques which are simple enough to be accessible to a wide user-base, yet sophisticated enough to yield precise datasets. The work adapts a traditional model for depth estimation, now allowing the increased spectral information delivered by WV2 to be accessed. I finish by explicitly quantifying the added capacity of WV2 over more traditional 4-band sensors. The results of this study support the widespread use of WV2 by the extensive community of managers and scientists that are tasked with mapping and monitoring coral reefs around the world.

Abstract

Information gathered by remote sensing systems is an important tool in the implementation and evaluation of conservation measures for coral reef ecosystems, and the launch of the Worldview-02 satellite in October 2009 improved coral reef researchers' capability to map these ecosystems. A basic, yet essential, mapping product for coral reef studies are bathymetric maps, and the increased spectral and spatial information provided by the Worldview-02 imagery improve optically-derived bathymetric maps. A standard model for optically-derived bathymetry was modified to include the increased spectral information that Worldview-02 imagery provides over previous satellites (e.g., QuickBird), and 63 versions of this model, each with a different combination of input variables, were compared using an information-theoretic approach. The model comparison demonstrated that a model containing the full set of input variables (6 band-ratios) provided the most reliable depth estimates even when ground-truth data were limited. It was also demonstrated that applying simple sun-glint removal and atmospheric correction techniques provided more reliable estimates of model parameters thereby improving precision of depth estimates. Finally, an accuracy assessment quantified the benefit provided by the modified model and increased spectral information, and it identified increased accuracy in depth estimates over seafloor features with high albedos. The results of this study support the use of Worldview-02 imagery in the mapping of near-shore coral reef systems in support of the implementation and assessment of conservation measures.

Introduction:

The health of coral reef ecosystems around the world has precipitously declined due to increased anthropogenic and natural stresses leading to calls for expanded actions to conserve the resources provided by these ecosystems and prevent further degradation (Gardner et al. 2003; Hughes et al. 2003). Marine spatial planning, which includes the establishment of marine protected areas, is the process of designing policies and that incorporate the spatial patterns inherent to ecosystems, and it is increasingly gaining attention as a tool in the conservation of marine ecosystems (Douvere 2008). Satellite-based imaging systems with spectral bands within the visible spectrum (400 – 700 nm) reliably provide information at spatial scales needed to implement spatially-based conservation actions for coastal locations (Andrefouet and Riegl 2004), and they enable observations of the benthos at greater spatial and finer temporal scales than those allowed through field observation alone (Lubin et al. 2001; Hochberg and Atkinson 2003; Hochberg et al. 2004).

Within the oligotrophic waters commonly occurring in reefal systems, bathymetric maps derived from remotely-sensed imagery estimate seascape topography down to depths of 25 m (Stumpf et al. 2003), improve marine spatial planning by improving habitat classification maps (Mumby et al 1998), and provide a surface representing the physical boundaries shaping water motion in hydrodynamic models that can be used to better understand how predicted changes in oceanic and atmospheric conditions will affect coral reef ecosystem health and resilience in the near future (Heron and Skirving 2004). The spectral information provided by the six Worldview-02 bands within the visible spectrum increase the amount of spectral information available for a study area thereby improving the quality of mapping products for near-shore reefal systems.

Bathymetric maps of the coastal seascape can be created using information gathered through either active or passive remote sensing (Lyzenga 1978; Stumpf et al. 2003; Brock et al. 2004); both of which have associated costs and benefits. Light detection and ranging (LiDAR) is an active remote sensing technology in which a laser detects the distance of the sensor to the target (Brock et al. 2004). Wavelengths in the blue-green spectrum allow the laser to penetrate the water column and provide highly reliable depth estimates at fine spatial scales. Conversely, passive remote sensing technologies rely on a combination of upwelling radiance in the visible light spectrum (400 – 700 nm) detected by a sensor and known physical parameters affecting light attenuation within the water column to model depth (Lyzenga 1978; Stumpf et al. 2003). Furthermore, satellite-based instruments cover larger areas over shorter time periods, have shorter return intervals, and can observe remote locations inaccessible by airborne LiDAR systems at the cost of decreased accuracy in depth estimates and coarser spatial resolution (Brock et al. 2004). Two common spectral bands on satellite-based sensors are the blue and green bands, and the combination of these two bands has been used to derive bathymetry from QuickBird (e.g., Hochberg and Atkinson 2004), IKONOS (e.g., Stumpf et al. 2003), and Landsat imagery (e.g., Liceaga-Correa and Euan-Avila 2002), which have similar, though not identical, spectral responses to the blue and green bands on the Worldview-02 satellite.

Given this demonstrated capability to derive depths in clear coastal waters using information provided by as few as 2 bands in the visible spectrum, the increased number

of water-penetrating spectral bands provided by the Worldview-02 (WV2) satellite (6 bands) should improve water-depth retrievals. This study's overall goal was to identify and quantify the benefit provided by the increased number of bands for depth estimation. The first goal of this study was to identify an optimal model for estimating bathymetry within a near-shore coral reef system based on the six water-penetrating bands and quantify the accuracy of this model. The second goal of this study was to identify an optimal level of pre-processing prior to water-depth derivation, and the final goal was to identify an optimal set of pre-processing steps and model to be used when ground-truth data are limited.

Methods:

Overview

To meet the study's goals, the WV2 imagery was pre-processed to at-sensor radiance values, to remove sun-glint, to estimate reflectance, and to remove atmospheric effects. LiDAR data overlapping with the WV2 image are the ground-truth for depth estimation. The first goal of identifying the best model for water-depth retrieval was met by selecting a 4-km by 4-km subset from the area overlapped by the LiDAR and WV2 data and comparing candidate models' fit to these data using an information-theoretic approach after each pre-processing step. The candidate models for each pre-processing step were aggregated and compared the approach to meet the goal of identifying the optimal set of pre-processing steps. These two goals represent an idealized situation in which ample ground-truth data are available; however, the sample size used to address these two goals was not realistic. Four more realistic sample sizes were used to compare model selection frequency for ten models, again using the information-theoretic approach, to meet the goal of identifying an optimal model with limited-ground-truth information. Finally, an accuracy assessment quantified both the precision of the best-fit model and its improvement over the more standard model.

Study location

The study location was a coastal area off-shore of Key Largo in the northern Florida Keys National Marine Sanctuary. The study area was chosen due to the presence of high resolution LiDAR data (USGS 2008) covering the majority of the seafloor. The area contains seafloor features (e.g., reefs, sea grass beds, sand flats) with spatial arrangement in depths from the intertidal to 15 m typical to those found in shallow, near-shore coral reef ecosystems around the world thereby providing a representative coastal area for assessing water-retrieval models.

Worldview-02 imagery

A WV2 image was delivered by Digital Globe with geometric corrections and 11-bit digital numbers (DN) at a 2-m spatial resolution and a nearest-neighbor resample kernel (Figure 1). The image was converted from DN to at-sensor radiance values (μW cm^{-1} sr^{-1} nm^{-1}) through ENVI Service Pack 2. A patch to correct a bug affecting estimated radiance values for WV2 data was applied to ENVI prior to the conversion. For the purposes of this study, bands in the visible spectrum (bands 1 through 6) were pre-processed from the initial radiance values to reflectance values and used for depth estimation. Bands 7 and 8 were not used during bathymetric derivation because sea-

water is opaque in the NIR region meaning these bands would provide no information useable for estimating depth. However, this opacity means these two bands are essential for acquiring the information on sea-surface state within a pixel necessary for sun-glint removal.

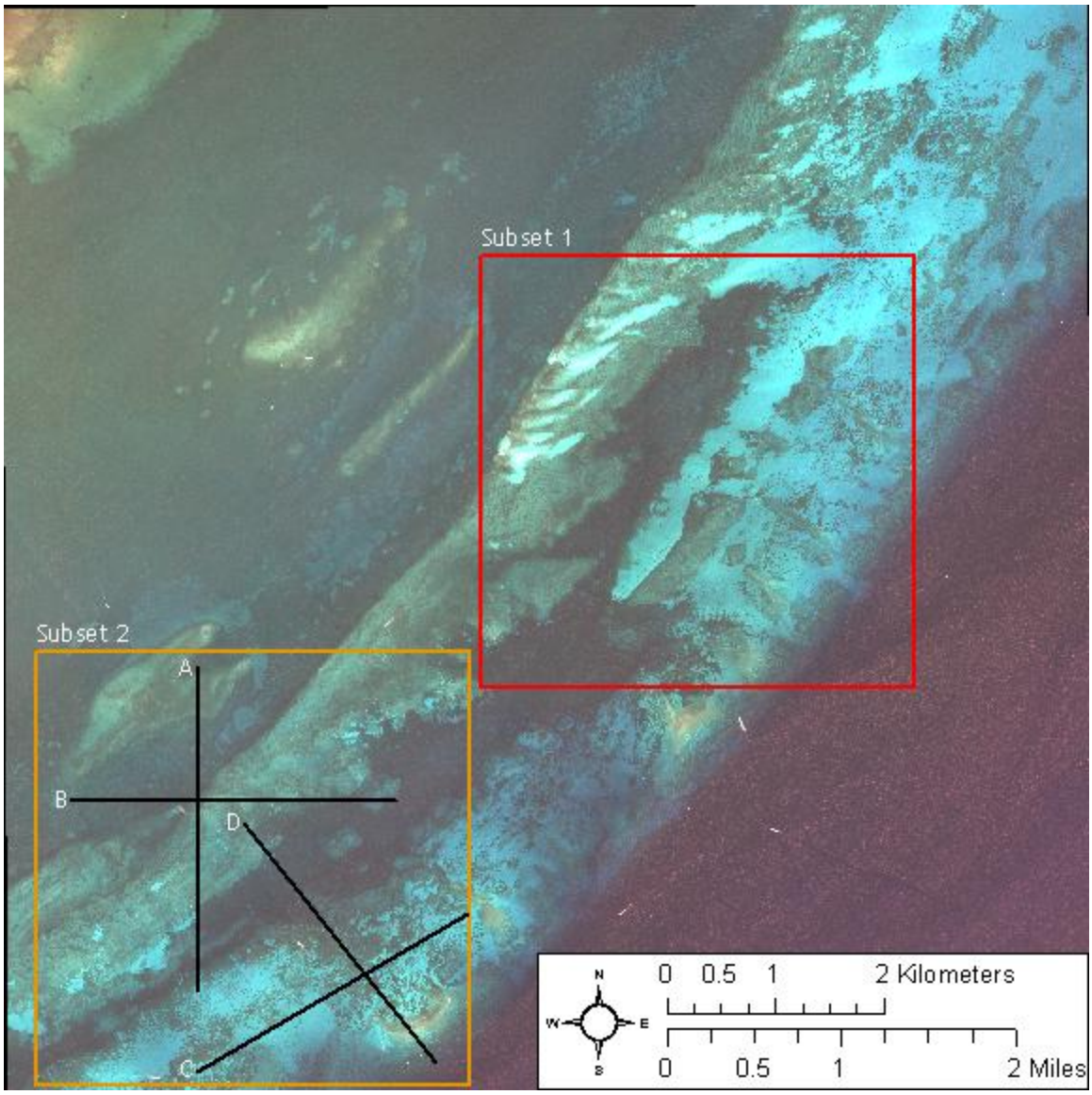

Figure 1: True color version of the WV2 image delivered by Digital Globe. Pixels from Subset 1 (red box) were used for model comparison to identify the overall best-fit model and best-fit model with limited ground-truth data. Subset 2 (orange box) and Transects A, B, C, D, and E (black lines) were used for accuracy assessments.

Initial investigation of the WV2 imagery showed a difference in the images created by the 'traditional' spectral bands, which are equivalent to QuickBird's 4 spectral bands (i.e., the blue, green, red, and NIR 1 bands), and the 'new' spectral bands provided by WV2 (i.e., the coastal, yellow, red-edge, and NIR 2 bands). Figure 2 shows an example of observed difference between band sets. The source of the difference was unknown, but the observed difference in boat wakes and sun-glint off of wave crests

indicated that the two band-sets observed different ocean-surface states. Thus, sun-glint removal and band-ratios for bathymetric derivation were limited to within the 'traditional' and 'new' band-sets to reduce potential effects of the different ocean surface states. For example, blue/green was a usable band combination, but the coastal/green combination was not usable because the two bands belong to different sets. For sun-glint removal, the NIR1 band was to estimate water surface properties in the blue, green, and red bands, and the NIR2 band similarly was used for the coastal, yellow, and red-edge bands.

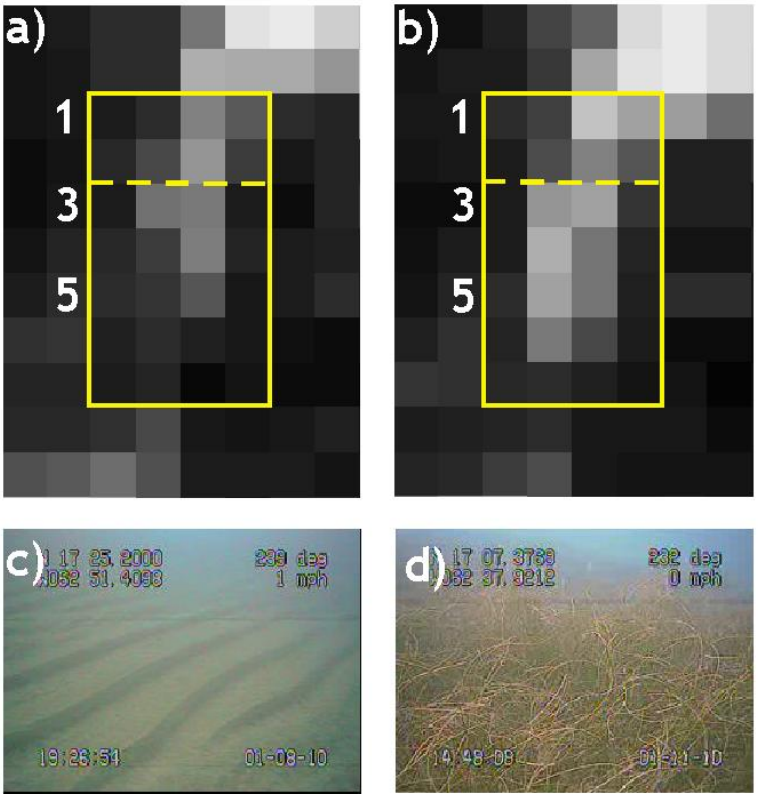

Figure 2: Close-up from the a) coastal and b) blue bands demonstrating the difference in pixel values between the 'traditional' and 'new' bands. Also provided are still images from video acquired by a drop-cam showing c) sand and d) dense sea grass. The top area in the yellow box (rows 1 and 2) is similar in both bands, but the bottom area (rows 3 to 7) has a different pattern in each band.

Sun-glint removal

Sun-glint was present in the WV2 image and was removed using the deglinting model of Hedley et al (2005), which generalized the methods of Hochberg et al (2003). The deglinting process was applied to the at-sensor radiance, L_t, values prior to estimating reflectance and correcting for atmospheric effects. The method first estimates a linear relationship between the visible band being corrected and a near infrared band through linear regression on a sample of deep-water pixels where sun-glint was present. The minimum NIR value, Min_{NIR}, from the sample, which represents the 'ambient,' non-glint NIR, is also identified. The radiance values are then corrected by

$$L_t' = L_t - b \cdot (L_{t,NIR} - Min_{NIR}) \quad (1)$$

where L_t' is the deglinted radiance value, b is the slope estimated by the linear regression, $L_{t,NIR}$ is the NIR radiance value, and Min_{NIR} is the minimum value for the near infra-red band established from the sample.

Apparent reflectance

Converting at-sensor radiance values to at-sensor reflectance, called apparent reflectance, prior to atmospheric correction is common because it represents the combined reflectivity of the atmosphere and surface system (Gao et al. 2009). Apparent reflectance, ρ_{obs}^{*}, is defined as (Gao et al. 2000, 2009)

$$\rho_{obs}^{*} \equiv \frac{\pi \cdot L_t}{\mu_0 \cdot F_0}, \tag{2}$$

where F_0 is the corrected extraterrestrial irradiance. The parameter μ_0 equals $1/\cos(\theta_0)$ where θ_0 is the sun azimuth angle.

Extraterrestrial irradiance at the top of the atmosphere is well quantified and varies with periodic change in the Earth-Sun distance due to orbital eccentricity and the Earth's tilt. This variation in extra-terrestrial irradiance is predictable, and Gordon et al. (1983) and Gregg and Carder (1990) estimated the corrected extraterrestrial irradiance for wavelength, $F_0(\lambda)$, as

$$F_0(\lambda) = E_0(\lambda) \cdot \left(1 + 0.0167 \cdot \cos\left[\frac{2\pi \cdot (D-3)}{365}\right]\right)^2 \tag{3}$$

where $E_0(\lambda)$ is the mean extraterrestrial irradiance for a wavelength and D is the Julian day of the year measured from 1 January. Extraterrestrial irradiance for band *i* is estimated as:

$$F_0 = \int_{\lambda_1}^{\lambda_2} F_0(\lambda) d\lambda \tag{4}$$

where λ_1 and λ_2 are the starting and ending wavelengths for band i, respectively.

Deep-water correction for atmospheric effects

The goal of atmospheric correction is to estimate atmospheric reflectance and remove its effect from apparent reflectance leaving reflectance from the water's surface and the sea floor (Gao et al. 2000). One way to estimate atmospheric effects is to use radiative transfer theory to model the absorption and scattering due to gases and aerosol particles (Gao et al. 2009); however, several issues contribute to increase the complexity of these models. Radiative transfer models for scatter due to aerosol particles estimate the number and size distribution of the particles. In maritime environments, the aerosol component is greater than over land, and the particles are heterogeneously distributed (Gregg and Carder 1990). Additional complications arise when short-term changes in ocean conditions that affect the aerosol component (e.g., surface roughness, wind speed) and the effects of scattering from adjacent pixels are considered. Several algorithms and modules for atmospheric correction that rely upon radiative transfer theory exist (e.g., FLAASH, 6S, Tafkaa); however, they require knowledge of many input parameters regarding the atmospheric and oceanographic conditions occurring at the time of image

acquisition (Adler-Golden et al. 2005; Gao et al. 2009), and they are not always available to those interested in atmospheric corrections. Relatively simpler, though less accurate, image statistic- based methods are available enabling those without access to the aforementioned algorithms and modules to correct for atmospheric effects. One such method is dark-body correction, which uses the known properties of a dark-body (e.g., ground cover in shadow or deep water) to estimate the 'ambient' atmospheric reflectance (Gao et al. 2009). Apparent reflectance can then be corrected to water-surface reflectance by subtracting the ambient atmosphere.

Formally, apparent reflectance, ρ^*_{obs}, is a combination of atmospheric reflectance, ρ^*_{atm}, seafloor reflectance, ρ^*_{sf}, and water-surface reflectance, ρ^*_g, such that

$$\rho^*_{obs} = \rho^*_{atm} + \rho^*_{sf} \cdot t + \rho^*_g \cdot t' \quad (5)$$

where t and t' are the transmittances through the water's surface and through the atmosphere, respectively. Atmospheric reflectance can be estimated if values for the apparent reflectance, the water-surface reflectance, and the seafloor reflectance are known. The apparent reflectance was estimated from the at-sensor radiance values and estimated extraterrestrial irradiance using Eq. 2, 3, and 4. Sea water reflectance is well described in the literature, and the reflectance described by Moral and Prieur (1977) was used for this value. Seafloor reflectance varies with benthic composition; however, deep waters can be assumed to have a seafloor reflectance equal to zero at all wavelengths allowing an image subset over deep-water to be used in estimating atmospheric reflectance.

LiDAR Digital Elevation Model

In 2006, a joint effort by the US Geological Survey (USGS), the National Aeronautics and Space Administration (NASA), and the National Parks Service (NPS) mapped the seafloor topography for an area within the Florida Keys National Marine Sanctuary (Figure 3) using the Experimental Advanced Airborne Research LiDAR (EAARL) system (USGS 2008), which uses a laser focused at the 532 nm wavelength (Bonisteel et al. 2009) to penetrate the water column and return depth estimates for the seafloor. The resulting digital elevation model (DEM) had a 1-m spatial resolution and a vertical accuracy of ± 15 cm for depth estimates. The EAARL DEM was re-projected from NAD83 to WGS84 using triangulation with 25 automatically selected ground control points in ENVI to match the WV2 image's projection and then resampled to a 2-m spatial resolution to match that of the WV2 image. Both the re-projection and re-sampling used a nearest neighbor resample kernal. The resampled DEM provided a 'ground-truth' data with which models for optical derivation of bathymetry were tuned and assessed for accuracy.

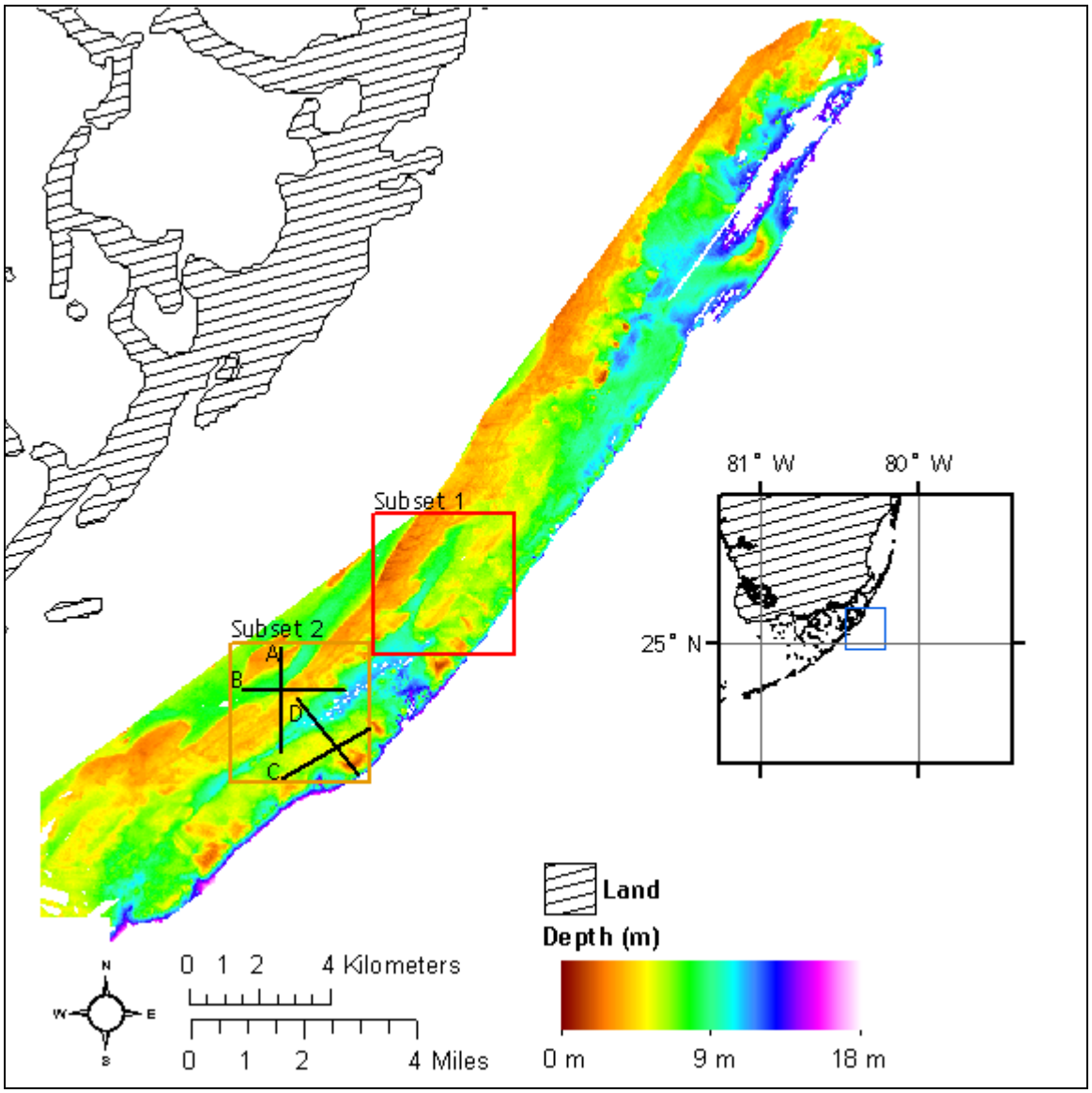

Figure 3: Digital elevation model created using the EAARL system (USGS 2008) and used as the 'ground-truth' depth values for the optically-derived bathymetry. Subsets 1 and 2, and Transects A through D shown in Figure 1 are also shown here.

Optically-derived bathymetry

According to Beer's Law, light attenuation in the water column increases exponentially as depth increases (Lyzenga 1978; Stumpf et al. 2003). Additionally, attenuation varies by wavelength resulting in less attenuation and greater depth penetration in the blue region of the visible spectrum than the green or red regions. These two properties are the basis for optically-derived bathymetry from multispectral, passive sensors used in this study. One standard model used to estimate depth from passively collected data is that of Stumpf et al (2003). In the Stumpf model, the estimated depth, Z^*, is related to the ratio of the natural logarithm for reflectance of two bands such that

$$Z^* = b_1 \cdot \frac{\ln(a \cdot \rho_i)}{\ln(a \cdot \rho_j)} - b_0 \quad (6)$$

where ρ_i and ρ_j are the reflectance values for bands *i* and *j*, and b_1, b_0, and a are constants. The constant a is set to ensure that the natural logarithm is positive and the ratio creates a linear response, and a value of 1000 was used for this study. The constants b_1 and b_0 are estimated by fitting a linear regression of the band-ratio to a set of corresponding ground-truth data points.

Equation 6 was modified in two ways for this study. The atmospheric correction and deglinting process resulted in reflectance values that were greater than or equal to 0 ($\rho^* \geq 0$); however, the natural log cannot be applied when the reflectance equals 0. Additionally, the ratio's denominator cannot equal 0. Thus, the first modification was to add the constant *e* within the natural log in both the numerator and denominator thereby ensuring that the minimum value for either was 1. The second modification was to expand the number of band ratios used for depth estimation. Thus, the general model for optically-derived bathymetry becomes

$$Z^* = b_n \cdot \bar{Z}_n + b_{n-1} \cdot \bar{Z}_{n-1} + ... + b_1 \cdot \bar{Z}_1 + b_0 \quad (7)$$

where

$$\bar{Z}_n = \frac{\ln(a \cdot \rho_i + e)}{\ln(a \cdot \rho_j + e)} \quad (8)$$

the constants $b_n, b_{n-1}, ..., b_1, b_0$ are estimated through multiple linear regression and $n, n-1, ..., 1, 0$ represent the *n*-th band-ratio. Eq. can be re-written as

$$Z^* = \sum_1^n b_n \cdot \bar{Z}_n + b_0 \quad (9)$$

where b_n is the estimated coefficient for *n*-th band ratio $\bar{Z}$. This final model essentially expands the model of Stumpf et al. (2003) from a linear regression to a multiple linear regression. This general model was used to estimate depth by creating band-ratios for the different band combinations enabled by the six WV2 bands in the visible spectrum. The models' results are compared using an information theoretic approach to identify the optimal model and the optimal level of pre-processing for bathymetric derivation.

Candidate models

The two sets of 'traditional' and 'new' bands allowed for six band-ratios (Table 1). In turn, these six band-ratios provided a complete set of 64 candidate models. One model uses no band-combinations thereby representing a situation where depth values were estimated by a purely random process. This was not a logical hypothesis in the current situation; therefore, this model was excluded from the model comparison resulting in 63 models for the comparison. These 63 candidate models were used to estimate depth from imagery with four levels of pre-processing: 1) no pre-processing, 2) deglinting only, 3) dark-water correction only, and 4) both deglinting and dark-water correction). The aggregation of the 63 models from the each of the 4 pre-processing levels resulted in a total of 252 models for the model comparison.

Table 1: Band ratios used in Eq. 9 for bathymetric derivation.

Band *i*	Band *j*	Band ratio
Blue	Green	$\bar{Z}_1$
Blue	Red	$\bar{Z}_2$
Green	Red	$\bar{Z}_3$
Coastal	Yellow	$\bar{Z}_4$
Coastal	Red-edge	$\bar{Z}_5$
Yellow	Red-edge	$\bar{Z}_6$

Model comparison

The combinations of various band-ratio inputs and pre-processing into the depth derivation model were compared using an information-theoretic approach based on Akaike Information Criterion (AIC; Akaike 1973; Burnham and Anderson 2003), which allowed the multiple competing models to be compared simultaneously. Each model represented a competing hypothesis that a given set of band ratios and pre-processing steps was the best model for estimating depth. Under this approach, an AIC value was calculated for each model (Akaike 1973), and a corrected AIC value (AIC_c) that adjusts for the number of estimable parameters was calculated for each model (Burnham and Anderson 2003). The candidate models were then ranked based on the (AIC_c) with the model with the lowest AIC_c value was considered the best-fit model and ranked 1. Based on the difference in AIC_c values between the best-fit model and the competing models (ΔAIC), an AIC weight (AIC_w) was calculated to quantify the evidence supporting the best-fit model.

Accuracy assessment

The standard blue/green combination and best-fit model were assessed for accuracy by comparing the depth values estimated by the models with the LiDAR depth values for a second subset. The root-mean-squared error (RMSE) and normalized RMSE (NRMSE) for the two models was calculated for pixels within Subset 2 and along Transects A, B, C, and D. These values provide an estimate of precision for each model, and a comparison quantified the increase in precision provided by the best-fit model.

Sample sizes

To identify the optimal model for depth derivation and the optimal pre-processing steps, a sample of pixels (n = 1,000,000) was randomly selected from a 4-km by 4-km area (N = 4,000,000; Subset 1; Figure 1). To address these two issues under more realistic conditions where sampled size was limited, Subset 1 was re-sampled 100 times for each of four sample sizes (n = 100; n = 1000; n = 10,000; n = 100,000), and the model selection frequency for the ten top ranked models were compared. These sample sizes are similar to those of (Purkis et al. 2008; Rowlands et al. 2009; Purkis et al. 2010) who used the Stumpf model for bathymetric derivation. For the accuracy assessment, a second 4-km by 4-km image subset (N = 4,000,000; Subset 2; Figure 1) was selected. Transects A, B, C, and D were also used for accuracy assessment, and their sample sizes were 1501 pixels, 1500 pixels, 1248 pixels, and 1110 pixels, respectively.

Results:

Best-fit model for optically-derived bathymetry

The overall best-fit model was the full model using reflectance values corrected for both sun-glint and atmospheric effects, and the blue/green band-ratio with sun-glint removal and deep-water correction was the best-fit model among models with a single band-ratio (Table 2). The full model was also the best-fit model within all the four levels of pre-processing. Of the models using a single band-ratio, the blue/green band-ratio was the best-fit model within three of the pre-processing levels, and the coastal/yellow band-ratio was the best-fit model within the fourth pre-processing level (Table 2). Seven of the top ten ranked models had both deglinting and dark-water correction applied prior to depth estimation indicating that this level of pre-preprocessing was optimal (Table 2).

Table 2: Model comparison results (AIC values, delta AIC, AIC weights) for the ten overall best-fit models (Ranks 1 through 10) and the best models using only one-band ratios for each level of pre-processing (Ranks 146, 210, 213, and 214). The AIC weight equals 1.00 for the Rank 1 model and equals 0.00 for all other models indicating that the evidence in the data fully supports the Rank 1 model as the best-fit model.

Rank	Input variables	Pre-preprocessing	AICc	ΔAIC	AIC_w
1	$\bar{Z}_1, \bar{Z}_2, \bar{Z}_3, \bar{Z}_4, \bar{Z}_5, \bar{Z}_6$	SGR, DWC	2041411.37	0	1.00
2	$\bar{Z}_1, \bar{Z}_2, \bar{Z}_3, \bar{Z}_4, \bar{Z}_5, \bar{Z}_6$	None	2118586.96	77175.59	0.00
3	$\bar{Z}_1, \bar{Z}_2, \bar{Z}_3, \bar{Z}_4, \bar{Z}_5, \bar{Z}_6$	SGR	2168722.00	127310.63	0.00
4	$\bar{Z}_1, \bar{Z}_2, \bar{Z}_3, \bar{Z}_4, \bar{Z}_5$	SGR, DWC	2211770.24	170358.87	0.00
5	$\bar{Z}_1, \bar{Z}_2, \bar{Z}_3, \bar{Z}_4, \bar{Z}_6$	SGR, DWC	2238162.50	196751.13	0.00
6	$\bar{Z}_1, \bar{Z}_2, \bar{Z}_3, \bar{Z}_4$	SGR, DWC	2249686.19	208274.82	0.00
7	$\bar{Z}_1, \bar{Z}_2, \bar{Z}_3, \bar{Z}_5, \bar{Z}_6$	SGR, DWC	2275131.93	233720.56	0.00
8	$\bar{Z}_1, \bar{Z}_3, \bar{Z}_4, \bar{Z}_5, \bar{Z}_6$	SGR, DWC	2276415.44	235004.06	0.00
9	$\bar{Z}_1, \bar{Z}_2, \bar{Z}_4, \bar{Z}_5, \bar{Z}_6$	SGR, DWC	2287107.95	245696.57	0.00
10	$\bar{Z}_1, \bar{Z}_2, \bar{Z}_3, \bar{Z}_6$	SGR, DWC	2291160.25	249748.88	0.00
146	$\bar{Z}_1$	SGR, DWC	2797353.22	755941.85	0.00
210	$\bar{Z}_4$	DWC	3046508.74	1005097.37	0.00
213	$\bar{Z}_1$	SGR	3054637.59	1013226.22	0.00
214	$\bar{Z}_1$	None	3059799.81	1018388.44	0.00

SGR - Sun-glint removal
DWC - Deep-water correction

Best-fit model with limited ground-truth data

Of the ten candidate models compared using the four test samples sizes, the three top ranked models in Table 3 had a combined model selection frequency greater than or equal to 97%. These three models all used the full model and differed only in the level of pre-processing applied prior to depth estimation. Individually, the full model with deglinting and deep-water correction (Rank 1 model in Table 2) was the most frequently

selected model (frequency ≥ 84%; Table 3). Together, the Rank 2 and 3 were occasionally selected as the best-fit model, and the seven other candidate models included in the comparison (Ranks 4 through 10 in Table 2) were rarely or never selected as the best-fit model (Table 3).

Table 3: Selection frequency for the models ranked 1 through 10 in Table 2. The full model with sun-glint removal and dark-water correction (Rank 1) was consistently the best-fit model, and the full-model with varying levels of pre-processing had a selection frequency greater than or equal to 97% for all four sample sizes.

Model (Rank)	No. Points			
	100	**1000**	**10,000**	**100,000**
1	84 %	100 %	94 %	89 %
2	4 %	0 %	2 %	6 %
3	9 %	0 %	4 %	5 %
4	1 %	0 %	0 %	0 %
5	0 %	0 %	0 %	0 %
6	0 %	0 %	0 %	0 %
7	1 %	0 %	0 %	0 %
8	0 %	0 %	0 %	0 %
9	0 %	0 %	0 %	0 %
10	1 %	0 %	0 %	0 %

Accuracy assessment

In general, the full model better estimated depth than the blue/green model; however, the full model suffered elevated errors when artificial objects (e.g., boats) contaminated pixels. For all pixels included in Subset 2 where LiDAR and WV2 imagery were both available (n = 3,920,674), the blue-green model had a greater precision in depth estimates (RMSE = 1.07 m; NRMSE = 7.64%) than the full-model (RMSE = 1.45 m; NRMSE = 10.29%); however, comparison of pixels with an error of less than 10 m between the observed and predicted depths (n = 3,920,392) in both models resulted in the full model having a higher precision (RMSE = 0.77 m; NRMSE = 5.49%) then the blue/green model (= 1.03 m; NRMSE = 7.32%; Figure 4). The sources of these errors were primarily boats and their wakes.

Comparisons of LiDAR depths and the predicted depths along Transects A, B, C, and D further demonstrated that the full model better predicted depth than the blue/green model (Figure 5). These comparisons also demonstrated that the blue/green model overestimated depth for shallow reef areas and underestimated depth for sandy areas. The full-model displayed a similar pattern but with a smaller magnitude in the errors between observed and predicted depths. This indicates that the greatest sources of error in depth retrievals for both models are submerged features with high albedos; however, the influence differs between models with the blue/green model incurring greater error than the full model.

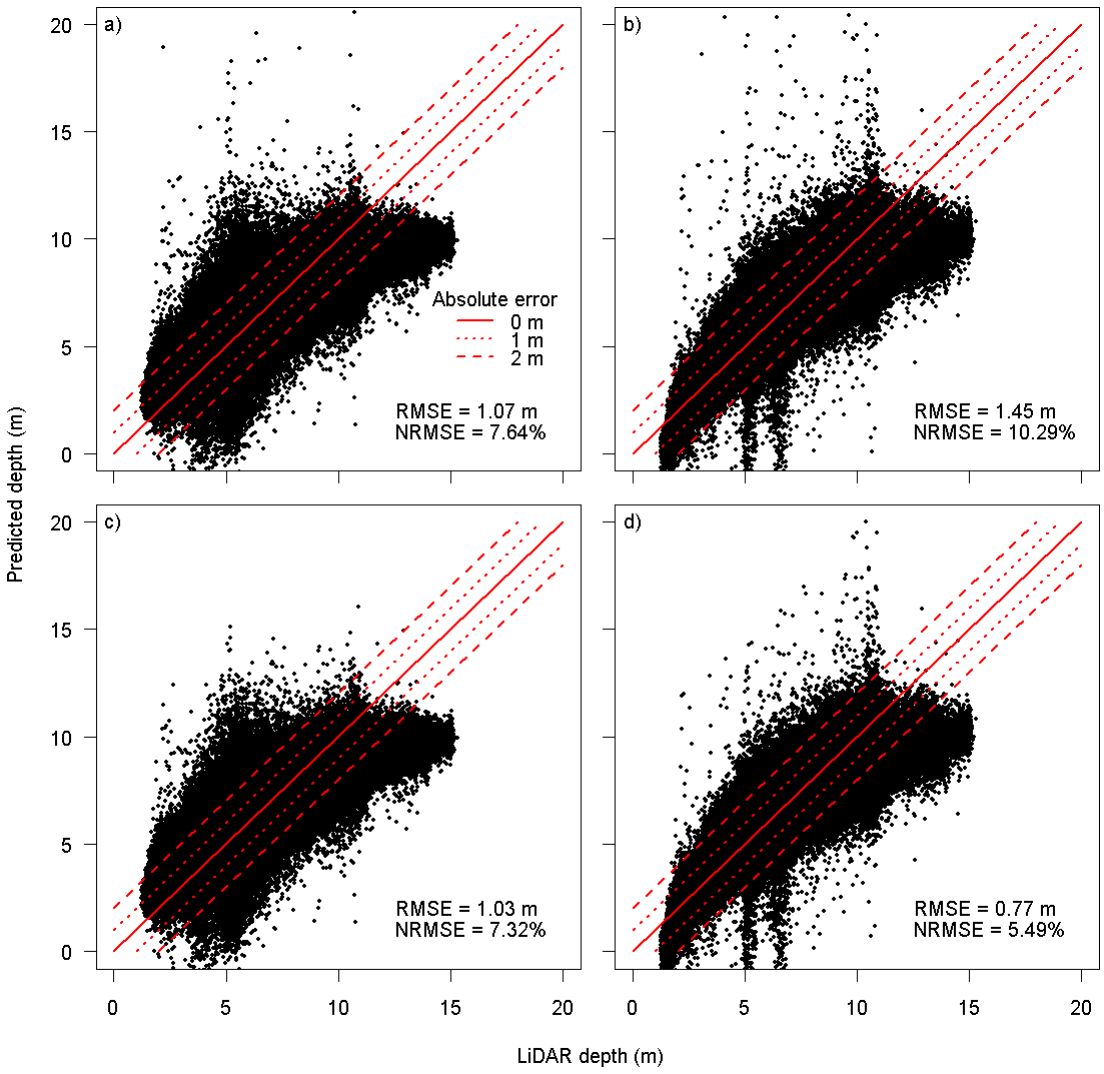

Figure 4: LiDAR depth and predicted depths for pixels in Subset 2 after deglinting and deep-water correction for a) the blue/green model and b) the full model and after removal of pixels with absolute errors greater than or equal to 20 m for c) the blue/green model and d) the full model. Lines provide references for absolute differences between the LiDAR depth and estimated depth of 0 m (i.e., no difference), 1 m, and 2 m.

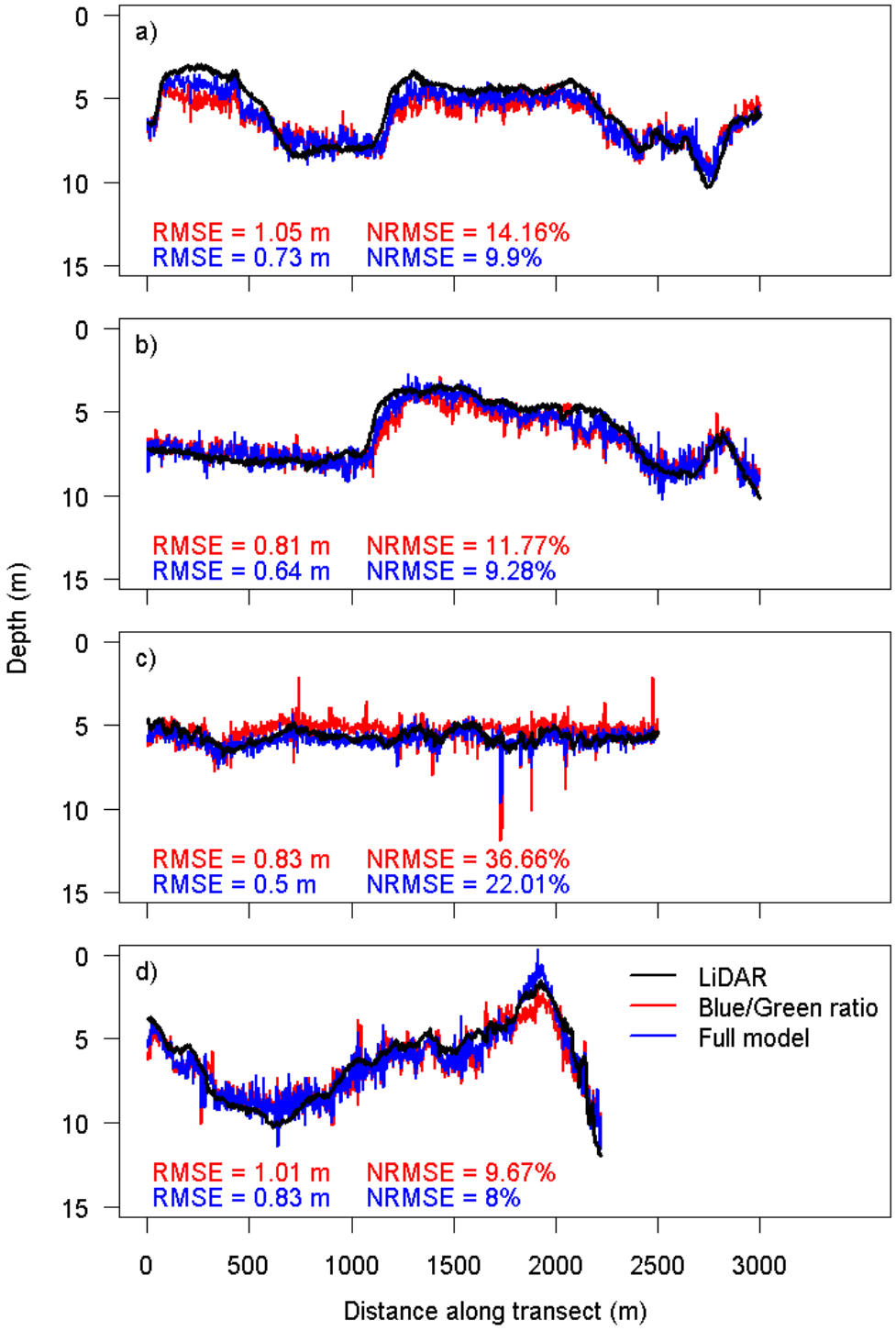

Figure 5: LiDAR depth (black line) with depth estimated by the blue/green band ratio (red) and the best-fit model (blue) along a) Transect A, b) Transect B, c) Transect C, and d) Transect D. The full-model better estimated depths for shallow reef areas (e.g., reef crests) and sand than the blue/green band-ratio, and it had a lower root-mean-squared error (RMSE) and normalized RMSE (NRMSE) indicating an improvement in depth estimation.

Discussion:

The WV2 satellite provides finer spatial resolution and more spectral information in the visible spectrum than previous satellites, positioning it as the forerunner for coral reef mapping. Prior to the launch of WV2 in 2009, QuickBird imagery had the finest spatial resolution for commercial satellites (~ 2.4 m) making it the satellite of choice for mapping coral reefs. This spatial resolution combined with three bands in the visible spectrum allowed near-shore reefal systems to be mapped and monitored in greater detail than had been previously possible. WV2 elegantly builds on the capabilities provided by QuickBird by increasing both the spatial resolution and available spectral information, and this increase in information provides greater detail for mapping coral reef ecosystems. The increased capabilities provided by the sensor however require a re-examination of established processing procedures, so as to ensure that the full capabilities of the WV2 imagery for reef mapping can be accessed. This study examined one such established method, optically-derived bathymetry using a band-ratio, and identified the new capacity provided by the additional bands.

This study demonstrates that expanding the Stumpf model to include a greater number of band-ratios, provides a better solution for optically-derived bathymetry. Such models have existed for over 30 years; Lyzenga (1978) developed the underlying theory and Lyzenga (2006) further developed the methodology resulting in a multiple linear regression similar to that used in this study. However, that model relies on knowing the optical properties of the water at the time of image acquisition. The model developed in Stumpf et al. (2003) built on the strategy developed by Lyzenga, but differed in that it used a ratio of the blue/green spectral bands for depth estimates. The upshot being that a reduced number of parameters now need to be estimated; two of which could be derived by fitting a linear regression of the band-ratio values to known depths. The uplift provided by the Stumpf model is that it enabled depth derivation in a greater number of situations, including those where accurate measurements of the water properties (e.g., turbidity), were unavailable. The model developed and evaluated in this study expands the Stumpf model from a linear regression to a multiple-linear regression, allowing for the increased amount of information provided in WV2 imagery to be included in the retrieval of water depth. The increased capacity provided by the WV2 imagery, coupled with the new model presented herein, has a greater precision in water-depth retrievals. More specifically, the derived depths over seafloor features with high albedos, such as sand and shallow reef tops, were more precise than could be achieved using more standard models and the 4 spectral bands of more traditional satellites.

This study affirms that deglinting and atmospheric correction methods should be applied to WV2 imagery prior to the development of bathymetric maps in order to increase the accuracy of the final products. Pre-processing methods alter the estimated radiance and reflectance values to account for known sources of error in the data, resulting in values that more closely estimate the true radiance and reflectance. Thus, it is not surprising that applying both pre-processing procedures prior to fitting the depth derivation model improved retrieved water-depths. The two procedures used in this study were relatively simple, and it is expected that more sophisticated correction models would further improve the resulting parameters estimates thereby improving depth retrievals. Therefore, a primary priority for users of WV2 data should be the adaptation

of pre-existing atmospheric correction algorithms that are applicable over both land and water targets for use with WV2 data.

Declines in the health of coral reefs around the world have led to increased calls for conservation and protection of these ecosystems (Gardner et al. 2003; Hughes et al. 2003), including the development of conservation actions rooted in marine spatial planning (Douvere 2008). Imagery acquired by the WV2 satellite increases the available spectral and spatial information within a target area, thereby increasing researchers' capability to map coral reef ecosystems. This increase in capability improves baseline information, monitoring of changes over time, and evaluation of conservation measures; all of which are vital to implementing and improving conservation efforts. WV2 imagery bridges gaps in coral reef mapping and conservation previously addressed by more traditional 4-band sensors, such as QuickBird, thus positioning the satellite as a vital tool in the near-term and long-term conservation of these threatened ecosystems. The development and launch of this satellite is a boon to the coral reef mapping community, and the information acquired by this sensor will improve the conservation of the goods and services provided by coral reef ecosystems.

References

Adler-Golden S, Acharya PK, Berk A, Matthew MW, Gorodetzky D. 2005. Remote bathymetry of the littoral zone from AVIRIS, LASH, and QuickBird Imagery. IEEE Transactions on Geoscience and Remote Sensing. 43(2):337-347.

Akaike H. 1973. Information theory as an extension of the maximum likelihood principle. In: Second International Symposium on Information Theory. BN Petrov and F Csaki (Eds.). Akademiai, Budapest.

Bonisteel JM, Nayegandhi A, Wright CW, Brock JC, Nagle DB. 2009. Experimental Advanced Airborne Research Lidar (EAARL) Data Processing Manual. U.S. Geological Survey Open-File Report, 2009-1078, 38p.

Brock JC, Wright CW, Clayton TD, Nayegandhi A. 2004. LIDAR optical rugosity of coral reefs in Biscayne National Park, Florida. Coral Reefs: 23:48-59.

Burnham KP and Anderson DR. 2002. Model selection and multimodel inference. Second edition. Springer-Verlag. New York.

Douvere F. 2008. The importance of marine spatial planning in advancing ecosystem-based sea use management. Marine Policy. 32:762-771.

Gardner TA, Cote IM, Gill JA, Grant A, Watkinson AR. 2003. Long-term region-wide decline in Caribbean corals. Science 301(5635):958-960.

Gao B, Montes M, Ahmad Z, Davis C. 2000. Atmospheric correction algorithm for hyperspectral remote sensing of ocean color from space. Applied Optics 39(6):887-896.

Gao B, Montes M, Davis C, Goetz AFH. 2009. Atmospheric correction algorithms for hyperspectral remote sensing data of land and ocean. Remote Sensing of Environment. 113:S17-S24.

Gregg and Carder. 1990. A Simple Spectral Solar Irradiance Model for Cloudless Maritime Atmospheres. Limnology and Oceanography. 35(8):1657-1675.

Hedley JD, Harborne AR, Mumby PJ. 2005. Simple and robust removal of sun glint for mapping shallow-water benthoc. International Journal of Remote Sensing. 26(10):2107-2112.

Heron SF and Skirving WJ. 2004. Satellite bathymetry use in numerical models of ocean thermal stress. Gayana. 68(2): 284-288.

Hochberg EJ and Atkinson MJ. 2003. Capabilities of remote sensors to classify coral, algae, and sand as pure and mixed spectra. Remote Sensing of Environment 85:174-189.

Hochberg EJ and Atkinson MJ. 2008. Coral reef benthic productivity based on the optical absorptance and light-use efficiency. Coral Reefs. 27(1):49-59.

Hochberg EJ, Atkinson MJ, April A, Andrefouet S. 2004. Spectral reflectance of coral. Coral Reefs 23(1):84-95.

Hughes TP, Baird AH, Bellwood DR, Card M, Connolly SR, Folke C, Grosberg R, Hoegh-Guldberg O, Jackson JBC, Kleypas JA, Lough JM, Marshall P, Nystrom M, Palumbi SR, Pandolfi JM, Rosen B, Roughgarden J. 2003. Climate change, human impacts, and the resilience of coral reefs. Science 301(5635):929-933.

Lubin D, Li W, Dustan P, Mazel CH, Stamnes K. 2001. Spectral signatures of coral reefs: features from space. Remote Sensing of the Environment 75:127-137.

Liceaga-Correa MA and Euan-Avila JI. 2002. Assessment of coral reef bathymetric mapping using visible Landsat Thematic Mapper data. International Journal of Remote Sensing. 23(1):3-14.

Lyzenga DR. 1978. Passive remote sensing techniques for mapping water depth and bottom features. Applied Optics. 17(3):379-383

Lyzenga DR, Malinas NP, Tanis FJ. 2006. Multispectral bathymetry using a simple physically based algorithm. IEEE Transactions on Geoscience and Remote Sensing. 44(8):2251-2259.

Morel A and Prieur L. 1977. Analysis of variations in ocean color. Limnology and Oceanography. 22:709-722.

Purkis SJ, Graham NAJ, Riegl BM. 2008. Predictability of reef fish diversity and abundance using remote sensing data in Diego Garcia (Chagos Archipelago). Coral Reefs. 27:167-178.

Purkis SJ, Rowlands GP, Riegl BM, Renaud PG. 2010. The paradox of tropical karst morphology in the coral reefs of the arid Middle East. Geology. 38(3):227-230

Rowlands GP, Goodman JA, Riegl BM, Renaud PG, Purkis SJ. 2009. Habitat mapping in the Farasan Islands (Saudi Arabia) using CASI and QuickBird imagery. Proceedings of the 11th International Coral Reef Symposium. Ft Lauderdale, Florida, 7-11 Jully 2008. Session number 17.

Stumpf RP, Holderied K, Sinclair. 2003. Determination of water depth with high-resolution satellite imagery over variable bottom types. Limnology and Oceanography 48(1, part 2):547-556.

[USGS] United States Geographical Survey [Last modified: 2008 April 21]. EAARL Submarine Topography – Florida Keys National Marine Sanctuary. [cited 2010 August 17]. Available from: http://pubs.usgs.gov/of/2007/1395/start.html